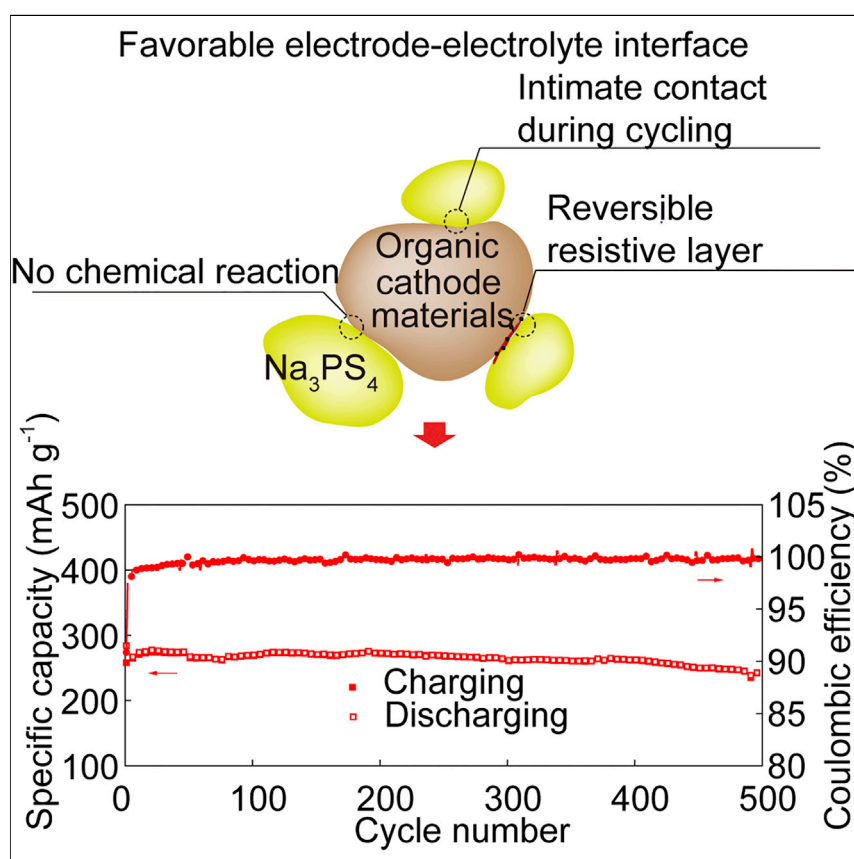


Article

Taming Active Material-Solid Electrolyte Interfaces with Organic Cathode for All-Solid-State Batteries



Forming compatible interfaces between cathode active materials and solid electrolytes is important for high-performance all-solid-state batteries. The organic cathode demonstrated here is (electro)chemically and mechanically compatible with a sulfide electrolyte. Its moderate redox potential enables the reversible formation of a resistive active material-electrolyte interface. It also maintains intimate contact with the electrolyte during cycling because of favorable mechanical properties. These features have contributed to the record cycling stability for all-solid-state sodium batteries.

Fang Hao, Xiaowei Chi, Yanliang Liang, ..., Kejie Zhao, Jun Lou, Yan Yao

yyao4@uh.edu

HIGHLIGHTS

All-solid-state sodium batteries with record cycling stability are demonstrated

Moderate potentials of organic cathodes render electrolyte decomposition reversible

Soft organic cathodes overcome mechanical contact failures with solid electrolytes

Hao et al., *Joule* 3, 1349–1359

May 15, 2019 © 2019 Elsevier Inc.

<https://doi.org/10.1016/j.joule.2019.03.017>



Article

Taming Active Material-Solid Electrolyte Interfaces with Organic Cathode for All-Solid-State Batteries

Fang Hao,^{1,5} Xiaowei Chi,^{1,5} Yanliang Liang,¹ Ye Zhang,¹ Rong Xu,² Hua Guo,³ Tanguy Terlier,⁴ Hui Dong,¹ Kejie Zhao,² Jun Lou,³ and Yan Yao^{1,6,*}

SUMMARY

Attaining stable active material-solid electrolyte interfaces is a great challenge in sulfide-based all-solid-state sodium batteries (ASSSBs). A resistive layer forms at the interface upon charging above the anodic stability potential of sulfide electrolytes. In addition, contact failure at the interface during cycling is long known, but a fundamental solution is not yet available. Herein, we use an organic cathode material, pyrene-4,5,9,10-tetraone (PTO), to enable high-performance ASSSBs. We report, for the first time, a reversible active material-electrolyte interfacial resistance evolution during cycling. We further show for the first time that a low-modulus cathode material such as PTO maintains intimate interfacial contact with solid electrolytes during cycling, thus improving cycle life. The PTO-based cells exhibit a high specific energy (587 Wh kg⁻¹) and a record cycling stability (500 cycles) among ASSSBs. This work reveals an effective cathode material design strategy toward compatibility with solid electrolytes and thus high-performance ASSSBs.

INTRODUCTION

All-solid-state sodium batteries (ASSSBs) with inorganic solid electrolytes feature higher safety and lower cost than non-aqueous liquid Li-ion batteries and are attracting worldwide attention for their potential use in large-scale energy storage applications.^{1–3} Among all currently known Na⁺-conducting solid electrolytes, sulfide-based electrolytes offer the necessary formability and conductivity.^{4–7} Despite these encouraging advantages, the development and application of sulfide-based ASSSBs have been advancing slowly because of serious issues concerning the interface between oxide cathode materials and sulfide electrolytes, as highlighted in Figure 1A. First, the redox potentials of oxide cathodes are far above the anodic decomposition potential of Na₃PS₄ (Figure 1C),^{8–10} which can result in the irreversible formation of a resistive layer at the interface, causing increased interfacial resistance and decreased capacity.^{11,12} Such detrimental reactions are accelerated in the presence of conductive carbon.^{13,14} Second, the chemical potential difference between oxide cathodes and Na₃PS₄ is large enough, leading to the formation of a highly resistive space-charge layer.¹⁵ Accordingly, electron-insulating coatings on the oxide cathodes by spray coating¹⁶ or atomic layer deposition,¹⁷ which are expensive to scale up, are commonly required to solve the abovementioned (electro)chemical issues. Third, oxide cathodes with high Young moduli (Figure 1D) are prone to induce high mechanical stress during cell cycling and lose interparticle mechanical contact with the electrolyte.^{18–20} Therefore, forming stable interfaces between cathode material and sulfide electrolyte is a critical task for the successful development of high-performance ASSSBs.²¹

Context & Scale

All-solid-state sodium batteries (ASSSBs) have been attracting considerable attention as safe and low-cost alternatives to Li-ion batteries. However, the performance of ASSSBs falls short of the requirements for commercial applications because of challenges concerning the electrode-electrolyte interface. Despite high Na-ion conductivity having been reported for solid-state sulfide electrolytes, most ASSSBs suffer a short cycle life. In this work, we show that an organic cathode material with a moderate redox potential enables an (electro)chemically reversible cathode-electrolyte interface. The unique elastic properties of organic cathode materials also ensure intimate contact during cycling. The benefits of organic cathode material are reflected in the excellent cell performance, providing insights to the electrode-electrolyte interface design in ASSSBs.



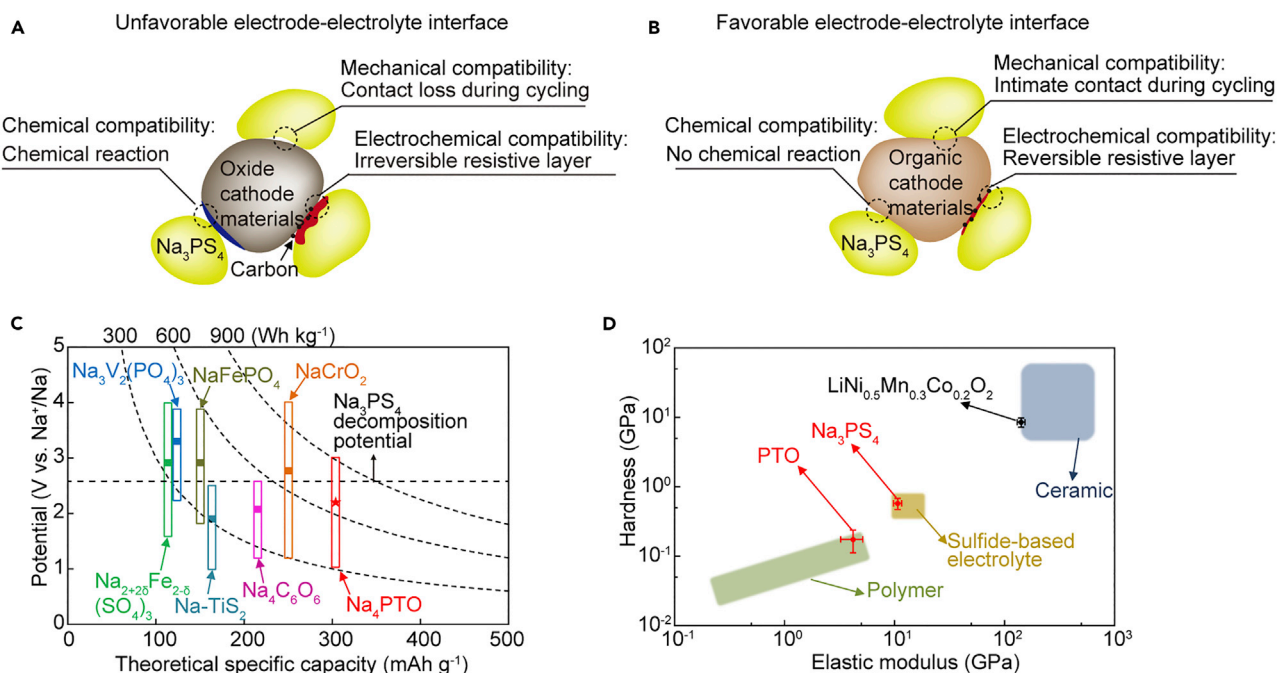


Figure 1. Interfacial Compatibility between Cathode Materials and Sulfide Electrolytes

(A) Unfavorable electrode-electrolyte interface between oxide cathode and Na_3PS_4 electrolyte leads to irreversible resistive layer formation, chemical reaction, and contact loss during cell cycling.
 (B) Favorable electrode-electrolyte interface between organic cathode and Na_3PS_4 electrolyte leads to reversible resistive layer formation, no chemical reaction, and intimate contact during cell cycling.
 (C) Redox potential versus theoretical specific capacity plot of reported intercalation-type cathode materials (TiS_2 ,^{6,40–43} $\text{Na}_3\text{V}_2(\text{PO}_4)_3$,^{44,45} NaFePO_4 ,⁴⁶ $\text{Na}_{2+2\delta}\text{Fe}_{2-\delta}(\text{SO}_4)_3$,⁴⁷ NaCrO_2 ,^{11,12,34} and $\text{Na}_4\text{C}_6\text{O}_6$) and PTO in this work. Theoretical specific capacities in this plot are calculated on the basis of cathode materials in the sodiated form. Solid squares and open bars represent the average redox potential and electrochemical window, respectively.
 (D) Hardness-modulus plot of electrode ($\text{LiNi}_{0.5}\text{Mn}_{0.3}\text{Co}_{0.2}\text{O}_2$,¹⁸ PTO) and electrolyte (ceramic, sulfide, and polymer) materials. The properties of PTO and Na_3PS_4 were measured in this work.

Cathode materials with moderate redox potentials and low Young moduli will thus be ideal candidates for overcoming the fundamental interfacial issues described above. Organic electrode materials represent one class of materials that is able to form a favorable electrode-electrolyte interface (Figure 1B) because of their unique tunable redox potentials^{22–25} and mechanical compliance. We have recently presented a tailored organic cathode $\text{Na}_4\text{C}_6\text{O}_6$ that is (electro)chemically compatible with Na_3PS_4 , thereby delivering a specific energy of 395 Wh kg^{-1} at the active-material level and a 70% capacity retention after 400 cycles, among the highest energy and longest cycle life for ASSSBs.²⁶ To further improve the specific energy, cathode candidates with even higher capacity and voltage are desirable but will also introduce new interfacial challenges. Here, we report another quinone, pyrene-4,5,9,10-tetraone (PTO),^{27,28} with a theoretical specific capacity of 409 mAh g^{-1} (or 303 mAh g^{-1} for the sodiated form Na_4PTO) and a higher working potential of 2.2 V (versus Na^+/Na). A notable difference of PTO from $\text{Na}_4\text{C}_6\text{O}_6$ is that its end-of-charge potential (3.1 V versus Na^+/Na) exceeds the anodic decomposition potential of electrolyte, resulting in partial oxidation of Na_3PS_4 . To address this challenge, we tweaked the carbon ratio in the composite cathode to achieve reversible Na_3PS_4 oxidation and reduction as revealed by *in-situ* electrochemical impedance spectroscopy (EIS), *ex-situ* X-ray photoelectron spectroscopy (XPS), and time-of-flight secondary ion mass spectrometry (ToF-SIMS) measurements. In addition, the Young modulus of PTO ($4.2 \pm 0.2 \text{ GPa}$; Figure S1) is approximately two orders of magnitude lower than that of oxide cathodes (100–200 GPa),²⁹ which

¹Department of Electrical and Computer Engineering and Texas Center for Superconductivity, University of Houston, Houston, TX 77204, USA

²School of Mechanical Engineering, Purdue University, West Lafayette, IN 47907, USA

³Department of Materials Science and NanoEngineering, Rice University, Houston, TX 77005, USA

⁴Shared Equipment Authority, SIMS laboratory, Rice University, Houston, TX 77005, USA

⁵These authors contributed equally

⁶Lead Contact

*Correspondence: yyao4@uh.edu

<https://doi.org/10.1016/j.joule.2019.03.017>

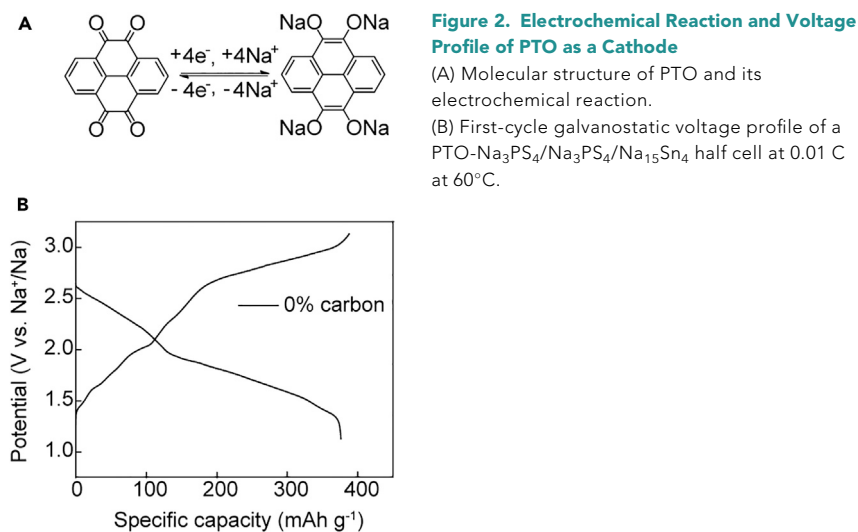


Figure 2. Electrochemical Reaction and Voltage Profile of PTO as a Cathode

(A) Molecular structure of PTO and its electrochemical reaction.

(B) First-cycle galvanostatic voltage profile of a PTO- $\text{Na}_3\text{PS}_4/\text{Na}_3\text{PS}_4/\text{Na}_{15}\text{Sn}_4$ half cell at 0.01 C at 60°C.

promises effective accommodation of interfacial stress and consistently intimate interfacial contact for solid-state batteries. These properties enable PTO-based cells to deliver a high specific energy (587 Wh kg^{-1}) and a record cycling stability (89% retention over 500 cycles) for ASSSBs reported to date (Table S1). The understandings obtained and the generalizable strategies established via the success of PTO make this work significant for energy storage.

RESULTS AND DISCUSSION

PTO molecule theoretically undergoes a four-electron transfer reaction that corresponds to a specific capacity of 409 mAh g^{-1} (Figure 2A). To experimentally verify the capacity of PTO but to minimize possible oxidation of Na_3PS_4 when charging above 2.7 V versus Na^+/Na , we first adopted a carbon-free composite cathode. We found that a half cell with the configuration of PTO- $\text{Na}_3\text{PS}_4/\text{Na}_3\text{PS}_4/\text{Na}_{15}\text{Sn}_4$ can deliver a reversible capacity of 376 mAh g^{-1} and a near-unity first-cycle Coulombic efficiency at a low rate (0.01 C) (Figure 2B). Next, to test at more practical current densities, composite cathodes with different carbon ratios (0, 5, 10, 20, 27, and 33 wt %) were prepared. Figures 3A and S2A show the first-cycle galvanostatic voltage profiles of the corresponding cells tested at 0.1 C. When no carbon was present, the cell only delivered 49% of its theoretical capacity, or 53% of that observed at 0.01 C, and a low Coulombic efficiency of 75%. When carbon was added, the charge capacity increased and reached a maximum of 314 mAh g^{-1} at 10 wt % carbon (Figure 3C). The first-cycle Coulombic efficiency increased as the carbon ratio increased from 0 to 5 wt % but then decreased as the carbon ratio increased further (Figure 3C). To elucidate the reasons for the low first-cycle Coulombic efficiencies, we have performed *in-situ* EIS (Figure S3A). The Warburg coefficient (A_w) was obtained from the slope of the $\text{Re}(Z)$ versus $\omega^{-1/2}$ relation and reflects the ionic diffusion resistance at the cathode-electrolyte interface.^{30,31} The A_w value of carbon-containing electrodes at the fully charged state (3.1 V versus Na^+/Na) monotonously went up as more carbon was present, along with the continuous decrease in Coulombic efficiency. We hypothesize that this phenomenon is due to the electrolyte oxidation in the presence of conductive carbon. To understand the carbon effect on overall cell performance, we used XPS to study the degree of electrolyte oxidation at different carbon ratios (Figure 3B). All samples showed two S 2p doublets at 160.7 (blue) and 161.9 eV (orange), corresponding to the P-S-Na and P=S bonds

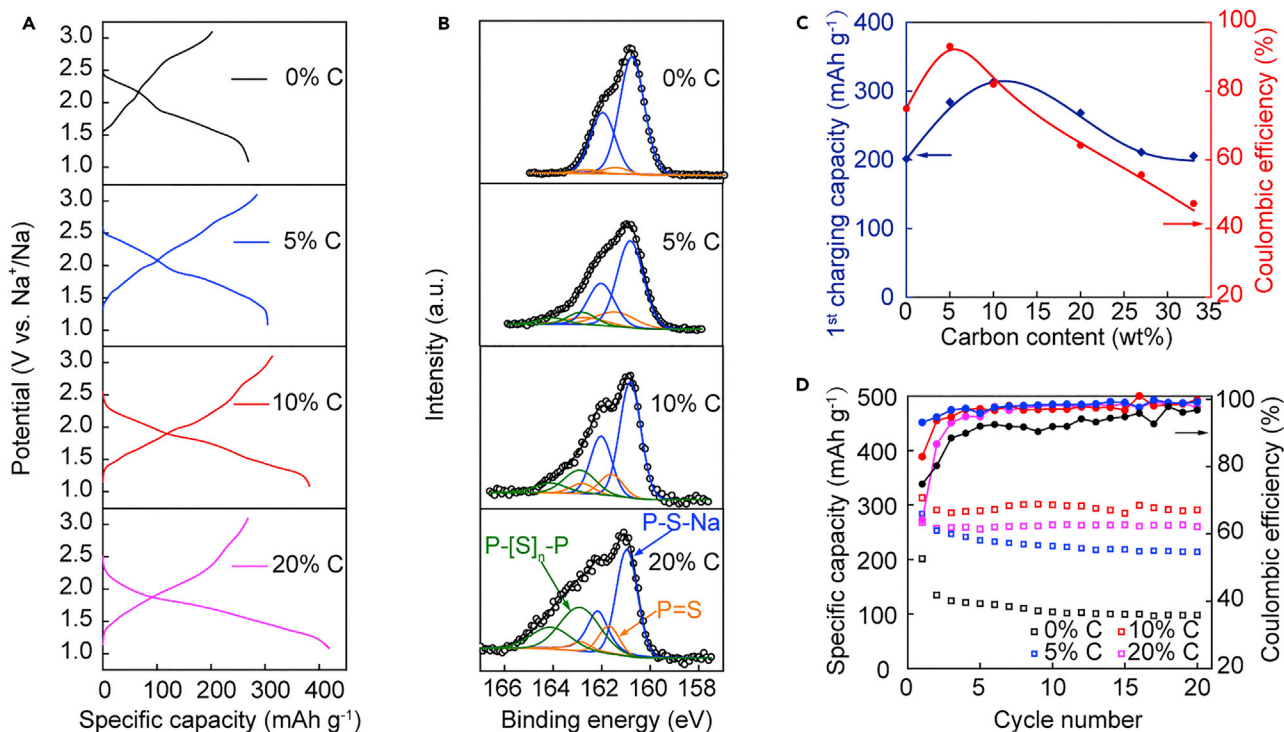


Figure 3. Effect of Carbon Ratio on the Electrochemical Performance of PTO-Based Half Cells at 0.1 C at 60°C

(A) First-cycle galvanostatic voltage profiles with various cathode composition (0, 5, 10, and 20 wt % C65 carbon [C]).

(B) XPS spectra (S 2p) of the composite cathodes at fully charged state after first cycle. Higher carbon ratio leads to more severe electrolyte oxidation.

(C) Plot of capacity and first cycle Coulombic efficiency dependence of carbon ratio.

(D) Charging capacity and Coulombic efficiency versus cycle number for the initial 20 cycles.

in Na_3PS_4 (Figure S4), respectively.^{26,32} When the carbon ratio was higher than 5 wt %, new peaks (green) appeared at a higher binding energy of 162.7 eV. According to a similar study on Li_3PS_4 from Janek's group,³³ we assigned these peaks to the P-[S]_n-P (n = 1, 2) bond in $\text{Na}_4\text{P}_2\text{S}_8$, $\text{Na}_4\text{P}_2\text{S}_7$, and $\text{Na}_2\text{P}_2\text{S}_6$, which are oxidation products of Na_3PS_4 . When the carbon ratio increased to 10 and 20 wt %, we saw that the intensity of the new peaks increased, indicating that more ionically resistive phases were produced. Therefore, the low efficiency for carbon-containing composite cathodes results from inefficient ionic conduction at the interface due to oxidation of Na_3PS_4 . On the other hand, the carbon-free electrode had the lowest A_w value of $1611 \Omega \text{ s}^{-1/2}$ but still low efficiency. As shown in Figure S3B, an additional semi-circle corresponding to a considerable charge-transfer resistance was observed at middle frequency, which likely associated with the electronically insulating nature of PTO (Figure S5), leading to a large total resistance despite the lowest A_w value. As a result, an increased charging overpotential was observed compared with that for charging at 0.01 C (Figure 2B), causing a premature end of charge and thus low Coulombic efficiency. The composite cathode with 10 wt % carbon showed the best combination of high initial charge capacity (314 mAh g^{-1}), first-cycle Coulombic efficiency (82%), and capacity retention (93% after 20 cycles) among the compositions investigated (Figures 3D and S2B). These observations suggest that (1) incorporation of carbon into the composite cathode is indispensable for providing sufficient electron transport and (2) too much carbon in the composite cathode causes significant accumulation of resistive products at the interface, thus leading to large capacity loss in the first cycle and the decreased discharge potential in first few cycles as shown in Figure S6. Therefore, composite cathodes with a mass ratio of

PTO:Na₃PS₄:carbon 2:7:1 and active material loading $\sim 1 \text{ mg cm}^{-2}$ were used in the following experiments. The mass loading of Na₁₅Sn₄ is 100 mg cm^{-2} . All cells were tested under 60°C and 0.5 MPa during cycling.

To probe the evolution of the cathode-electrolyte interface, we performed *in-situ* EIS measurements for PTO-based cells in the first three cycles. Each EIS measurement was preceded by a rest period of 30 min to allow for reaching equilibrium. Figure 4A shows the galvanostatic voltage profiles and the A_w extracted from the low-frequency EIS spectra (1.0–0.1 Hz) at each selected potential (Figures 4B, 4C, and S7; Table S2). During the first cycle, A_w decreased from $225 \Omega \text{ s}^{-1/2}$ (corresponding to a Na-diffusion coefficient D_{Na^+} of $1.46 \times 10^{-11} \text{ cm}^2 \text{ s}^{-1}$) at open circuit to $47 \Omega \text{ s}^{-1/2}$ at 1.1 V versus Na⁺/Na during discharge and then gradually increased to $154 \Omega \text{ s}^{-1/2}$ at 2.5 V versus Na⁺/Na during charge. Once it reached 2.8 V versus Na⁺/Na, above the decomposition potential of Na₃PS₄, we saw a significant increase of A_w to 550 and further to $1897 \Omega \text{ s}^{-1/2}$ (D_{Na^+} of $1.73 \times 10^{-12} \text{ cm}^2 \text{ s}^{-1}$) at 3.1 V versus Na⁺/Na. Interestingly, A_w reverted to $45 \Omega \text{ s}^{-1/2}$ at 2.0 V versus Na⁺/Na during the second discharge and remains low until the next charging process. The same impedance evolution was observed during the second and third cycles. It is noteworthy that even though PTO's end-of-discharge potential of 1.1 V versus Na⁺/Na exceeds the thermodynamic cathodic decomposition potential of Na₃PS₄ (1.55 V versus Na⁺/Na),⁸ A_w values stayed low at 1.5 V, 1.3 V, and 1.1 V versus Na⁺/Na, indicating that the probable cathodic instability at PTO-Na₃PS₄ interface does not produce a resistive passivation layer and further degrading the performance.

Therefore, we observed for the first time a reversible interfacial resistance evolution during cell cycling. Such a reversible behavior is the consequence of reversible conversion between conductive Na₃PS₄ phase and resistive phases, which occurs within the operation potential range of PTO (1.1–3.1 V versus Na⁺/Na). In contrast, oxide cathode materials with higher operation potentials, e.g., NaCrO₂ (up to 4.0 V versus Na⁺/Na), result in the irreversible formation of low conductivity species such as S⁰ at higher voltages,³³ which is responsible for capacity fading.

As the Na₃PS₄ decomposition also contributes to the cathode capacity, a control cell with a composite cathode containing only Na₃PS₄ and carbon was fabricated to quantify the contribution. As shown in Figure 4D, Na₃PS₄ alone showed a specific capacity of less than 20 mAh g⁻¹. Therefore, we can conclude that the high specific capacities of PTO-based composite cathodes were mainly contributed by PTO. To provide direct evidence of the identity and reversibility of oxidation products of Na₃PS₄, we conducted *ex-situ* XPS and ToF-SIMS on two cycled cells as shown in Figures 4E and 4F. The S 2p XPS spectra of the composite cathode after the third charge showed new peaks (green) that corresponded to the P-[S]_n-P bond, indicating partial oxidation of Na₃PS₄. After the following discharge, these peaks disappeared and the S 2p spectra became similar to that of pristine Na₃PS₄ (Figure S4). The ToF-SIMS spectra of the fully charged electrode showed peaks at 277, 387, and 399 m/z corresponding to NaP₂S₆⁻, Na₃P₂S₈⁻, and CNa₃P₂S₈⁻, respectively, indicating the formation of Na₂P₂S₆ and Na₄P₂S₈. None of these peaks retained after the fourth discharge, indicating a reversible transformation of the oxidized products back to Na₃PS₄. Overall, Na₃PS₄ oxidation and Na₄P₂S₈/Na₂P₂S₆ reduction are highly reversible between 1.1 and 3.1 V versus Na⁺/Na, guaranteeing a reversible interface that is beneficial for cycling stability of cells.

Because of the suitable deformability of sulfide electrolytes,⁷ intimate interparticle contact can be achieved for most composite cathodes containing sulfide

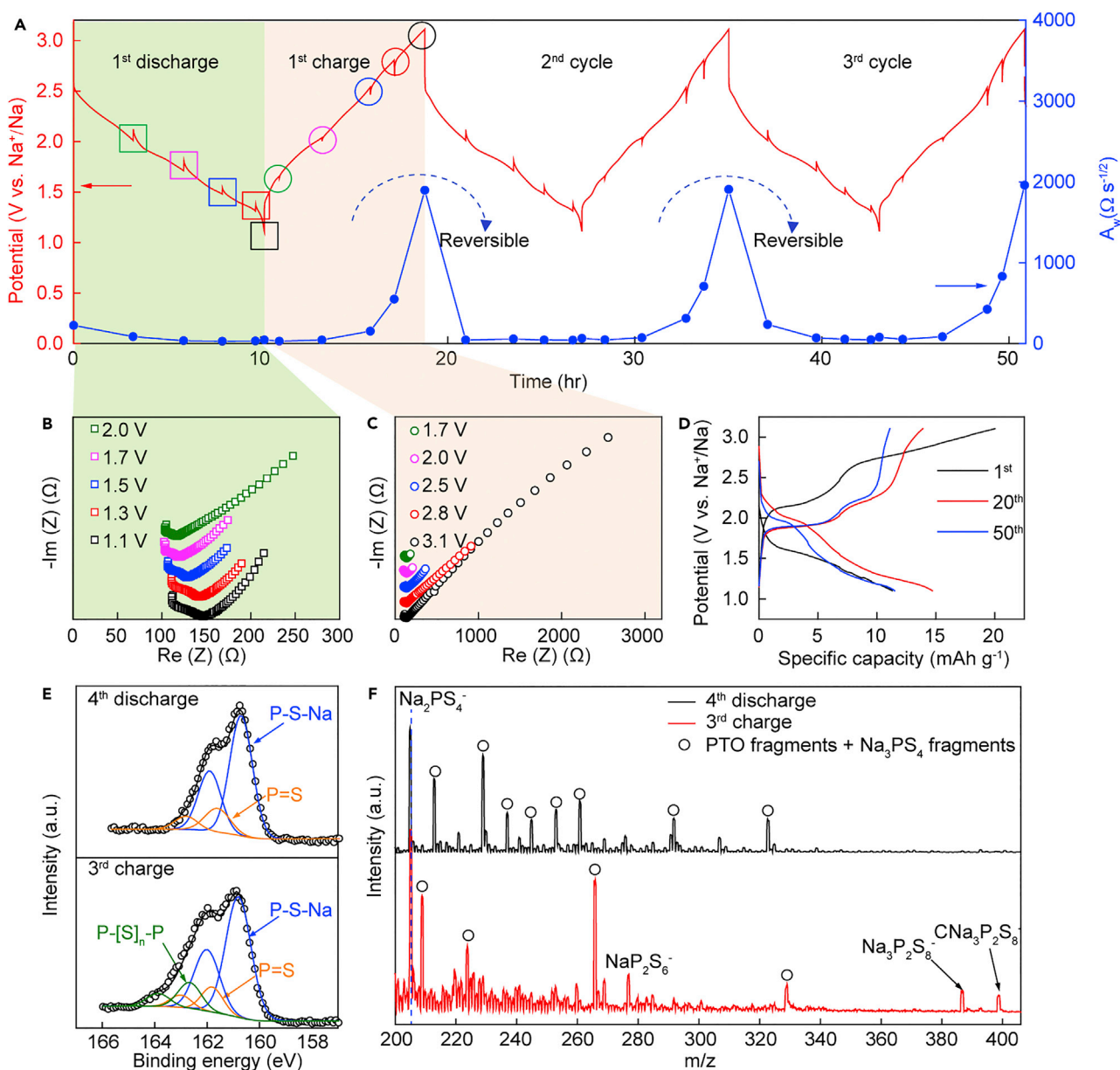


Figure 4. Investigation of Reversible PTO-Na₃PS₄ Interface Using EIS, XPS, and ToF-SIMS Analysis

The composite cathode has 10 wt % carbon and cycling at 0.1 C at 60°C.

(A) Intermittent galvanostatic voltage profile for first three cycles. Warburg coefficient is extracted from the low-frequency impedance spectra shown in (B) and (C).

(B and C) Impedance spectra recorded during (B) first discharge and (C) first charge.

(D) Galvanostatic voltage profile without PTO in the composite cathode.

(E) XPS spectra (S 2p) of the composite cathodes at fully discharged and charged states. The observed P-[S]_n-P bond at charged state disappeared at the following discharged state.

(F) ToF-SIMS spectra of the composite cathodes at fully discharged and charged states. The NaP₂S₆⁻, Na₃P₂S₈⁻, and CNa₃P₂S₈⁻ signals at fully charged state disappeared at the following discharged state.

electrolytes by simple cold pressing. Additionally, solution-processed solid electrolyte can create a uniform coating around the cathode particles to achieve intimate interparticle contact.³⁴ However, maintaining such an intimate contact upon cycling is challenging for oxide cathodes, which have high Young moduli. Stress-induced

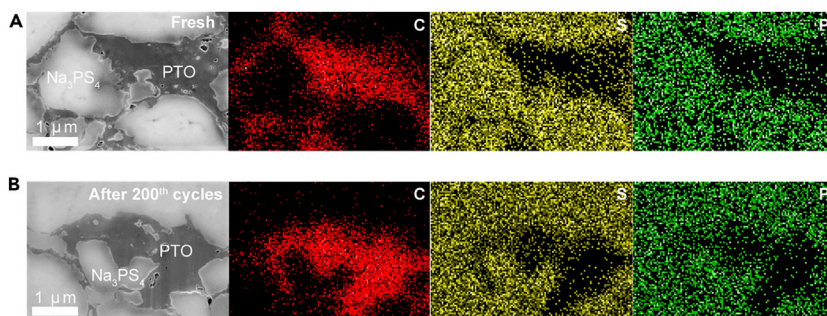


Figure 5. Cross-Sectional SEM Images and Elemental Mapping of FIB-Milled Composite Cathodes

(A) Before cycling.

(B) After 200 cycles. The intimate interparticle contact is maintained well after cycling. No obvious cracks are found in the cycled cathode.

cracks were observed in cycled cathodes at the active material particle-electrolyte interface.¹⁹ In contrast, PTO shows intimate contact with Na₃PS₄ before (Figure 5A) and after 200 cycles (Figure 5B), which is attributed to the small Young modulus of PTO that helps the particles readily accommodate the mechanical stress generated at the interface upon cycling. The cell therefore shows 304 mAh g⁻¹ specific capacity at 0.1 C with 97% capacity retention after 100 cycles (Figure S8). To the best of our knowledge, this consistently intimate interfacial contact is revealed for the first time for solid-state batteries. Low-modulus electrode materials should receive more attention as an effective approach to mitigate capacity fading originated from mechanically induced contact loss.

Size effect of electrode materials on the battery kinetics is well known.^{35,36} Smaller electrode particles lead to shorter ionic and electronic pathways. Therefore, we prepared PTO micropellets (PTO-MPs) and PTO nanorods (PTO-NRs) by mechanical milling and a chemical antisolvent precipitation method, respectively. Scanning electron microscopy (SEM) images in Figures 6A–6C show a significant particle size reduction: bulk PTO (PTO-B) particles are 50–100 μm in diameter, while PTO-MP has an average diameter of 5 μm and a thickness of 1 μm, and PTO-NR is ~1 μm in length and ~300 nm in thickness. The Fourier transform infrared (FTIR) spectra (Figure S9) show an identical profile, indicating no change in molecular structure during downsizing. The rate performance of differently sized PTO is shown in Figures 6D–6G. PTO-NR exhibited the best rate capability, with capacity of 322 mAh g⁻¹ at 0.1 C and 200 mAh g⁻¹ at 1 C. PTO-NR allows the cell to achieve a specific energy of 587 Wh kg⁻¹ at 0.1 C, a specific power of 335 W kg⁻¹ at 1 C, (Figure 6H), and 89% capacity retention after 500 cycles at 0.3 C (Figure 6I). It is noteworthy that forming stable interfaces between anode materials and sulfide electrolyte is also important.³⁷ We observed gradually increasing overpotential in a Na₁₅Sn₄/Na₃PS₄/Na₁₅Sn₄ symmetric cell (Figure S10A), which agreed with the unstable Na-Sn alloy-Na₃PS₄ interface as reported by other groups.⁸ The degradation of the Na₃PS₄-Na₁₅Sn₄ interface may be responsible for the gradual capacity fade (Figure S10B). Further improvement of the cycling stability would require simultaneous progress in developing the stable anode-electrolyte interface.

In summary, we have demonstrated the capability of an organic cathode material PTO to enable high-energy, high-power, and long-cycle-life ASSSBs. We tweaked the carbon ratio in the composite cathode to achieve the best combination of high initial charge capacity, first-cycle Coulombic efficiency, and capacity retention. We also observed, for the first time, a reversible cathode-electrolyte interfacial resistance

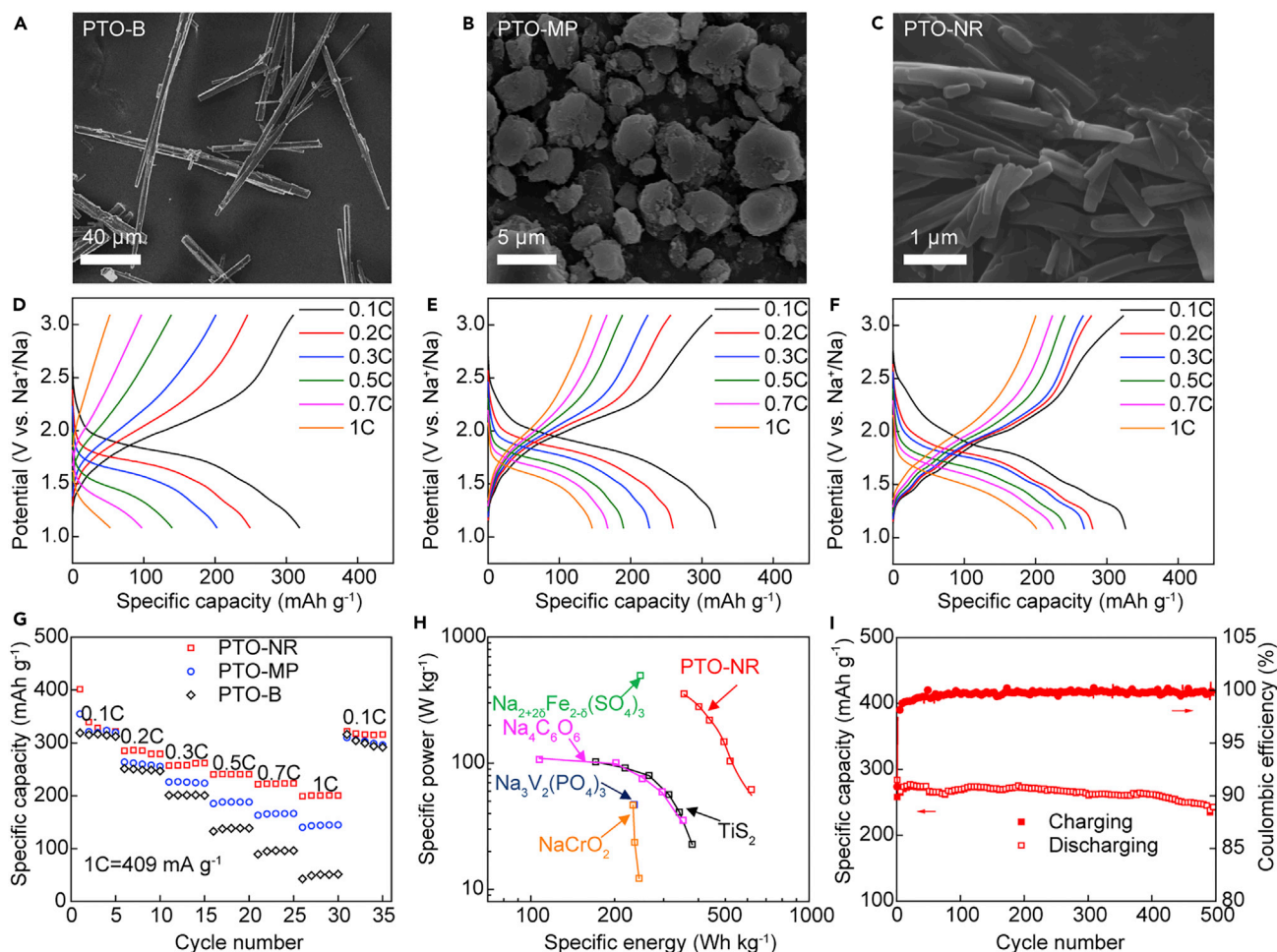


Figure 6. Morphology of PTO in the Form of PTO-B, PTO-MP, and PTO-NR and their Corresponding Electrochemical Performance with 10 wt % Carbon at 60°C

(A–C) SEM images of PTO-B (A), PTO-MP (B), and PTO-NR (C).

(D–F) Galvanostatic voltage profiles of cells with PTO-B (D), PTO-MP (E), and PTO-NR (F) at different current densities (1 C = 409 mA g⁻¹).

(G) Rate capabilities with varying PTO particle size in the composite cathodes.

(H) Ragone plot comparing previously reported intercalation-type cathode materials (TiS₂,^{6,40–43} Na₃V₂(PO₄)₃,^{44,45} Na_{2+2δ}Fe_{2-δ}(SO₄)₃,⁴⁷ NaCrO₂,^{11,12,34} and Na₄C₆O₆²⁶) and PTO-NR.

(I) Capacity and Coulombic efficiency versus cycle number for PTO-NR-based cell at 0.3 C.

evolution during the cell cycling. We have further shown that PTO with a Young modulus two orders of magnitude smaller than that of oxide cathodes is capable of overcoming mechanical failures and maintaining intimate interparticle contact upon cycling. As a result, reversible resistance and intimate contact at the electrode-electrolyte interface form the basis of achieving record specific capacity and cycling stability of any ASSSBs reported to date. The improved performance and deeper understanding of the electrode-electrolyte interface are shaping up a bright future for ASSSBs and opening up new opportunities for other solid-state devices.

EXPERIMENTAL PROCEDURES

Synthesis

Na₃PS₄ glass-ceramic powders were prepared via mechanochemical reaction and heat treatment. In brief, 1.02 g of Na₂S (Alfa Aesar, 99.9%) and 0.98 g of P₂S₅

(Sigma-Aldrich, 99%) were ball milled in a 250 mL argon-protected stainless-steel jar containing stainless-steel milling balls (2 × Φ 15 mm and 20 × Φ 10 mm) at 500 rpm for 2 h to obtain amorphous powders, which was further treated under vacuum at 260°C for 2 h to obtain glass-ceramic Na₃PS₄. Na₃PS₄ has been shown unstable with Na metal³²; therefore, a Na₁₅Sn₄ alloy (~0.1 V versus Na⁺/Na) was prepared following the literature.³⁸ PTO-B was synthesized following the previous report.²⁸ PTO-MP was prepared by ball milling 200 mg of PTO powders in a 100 mL agate milling jar at 400 rpm for 10 h. PTO-NR was synthesized using a chemical antisolvent precipitation method. Briefly, 50 mg of PTO-B was dissolved in 13 mL of tetrahydrofuran (THF, anhydrous, ≥99.9%, Sigma-Aldrich) and quickly injected into 70 mL of deionized water. After sonication for 10 min, yellow precipitates were collected by centrifuging at 10,000 rpm for 15 min and subsequent vacuum drying overnight.

Materials Characterization

Nanoindentation measurements were performed on the surface of cold-pressed Na₃PS₄ and PTO pellets using a nanoindenter (G200, Agilent Technologies) in an argon-filled glove box. The modulus and hardness were extracted from the load-displacement curves according to the standard Oliver and Pharr method.³⁹ Indentations under displacement control at a maximum depth of 1,000 nm were conducted at 10 different locations using a standard Berkovich tip. The loading, holding, and unloading time is 10 s, 5 s, and 10 s, respectively. The cross sections of composite cathodes utilized for SEM were observed in a focused ion beam (FIB)-SEM (FEI, Helios NanoLab 660 DualBeam) using an argon-ion beam polisher. Chemical information was obtained by FTIR spectroscopy (Nicolet iS5). The surface composition of the cycled composite cathodes was investigated by XPS (Physical Electronics PHI 5700) and ToF-SIMS (ION-TOF). All reported binding energy values were calibrated to the C 1s peak at 284.8 eV. A sputtering ion beam (Cs⁺ with 1 keV ion energy) was used for depth profiling of ToF-SIMS in negative polarization mode. To minimize air exposure, all samples were transferred from an argon-filled vessel to the analysis chamber.

Fabrication of All-Solid-State Cells

The PTO-Na₃PS₄-C composite cathodes were mixed using an agate mortar and pestle with weight ratios of 20:(80 - x):x, where the x values are 0, 5, 10, 20, 28, and 33. The Na₃PS₄-C composite cathode was mixed with a weight ratio of 70:10. To assemble the cell, 150 mg of electrolyte powder was filled into a polyetherether-ketone (PEEK) cell die with a diameter of 13 mm and pressed at a pressure of 75 MPa to form a pellet. 5 mg of the composite cathode (active material loading ~1.0 mg) was uniformly distributed on one side of the Na₃PS₄ pellet, and Na₁₅Sn₄ powder (100 mg) was added to the other side of the pellet and then pressed together at a pressure of 375 MPa. The over-dimensioned Na₁₅Sn₄ was necessary for fabrication as the Na₁₅Sn₄ layer easily cracked after cold pressing at such high pressure if less Na₁₅Sn₄ was used. During the cell testing, the cell was subjected to a torque of 20-inch-pound on each of three screws, corresponding to an initial pressure of ~0.5 MPa applied on the cell.

ELECTROCHEMICAL MEASUREMENTS

All galvanostatic discharge-charge cycles were performed in the potential range of 1.1–3.1 V versus Na⁺/Na at 60°C using a battery tester (LAND CT-2001A). Specific capacity is calculated based on the mass of active material in the composite cathode. EIS measurements were carried out using an electrochemical workstation (VMP3, Bio-Logic Co.) during galvanostatic cycling at the following potentials: 2.0 V, 1.7 V, 1.5 V, 1.3 V, and 1.1 V versus Na⁺/Na during the discharge process; and

1.7 V, 2.0 V, 2.5 V, 2.8 V, and 3.1 V versus Na⁺/Na during the charge process. Each measurement was preceded by a rest period of 30 min for equilibrium. A bias of 5 mV was applied for the measurement in the frequency range of 1.0 MHz to 0.1 Hz.

SUPPLEMENTAL INFORMATION

Supplemental Information can be found online at <https://doi.org/10.1016/j.joule.2019.03.017>.

ACKNOWLEDGMENTS

We thank the Solid Sodium team led by Prof. Steve Martin of Iowa State University for insightful technical discussions. We acknowledge the funding support from the U.S. Department of Energy's Advanced Research Projects Agency-Energy (ARPA-E) (award no. DE-AR0000654), UH Technology Gap Fund, and UH High Priority Area Large Equipment Fund. We acknowledge the support of the National Science Foundation for access to the ToF-SIMS at Rice University, supported through CBET1626418. ToF-SIMS analyses were carried out with support provided by the Shared Equipment Authority at Rice University.

AUTHOR CONTRIBUTIONS

Y.Y., F.H., and X.C. initiated this research and designed the experimental work. F.H., X.C., and Y.Z. synthesized the Na₃PS₄ electrolyte, conducted electrochemical measurements, and analyzed the results. Y.Z. and Y.L. participated in data analysis and discussion. R.X. and K.Z. conducted the nanoindentation measurements and mechanical property analysis. H.G. and J.L. performed the FIB-SEM measurements. T.T. conducted the ToF-SIMS measurements and analysis. H.D. synthesized the PTO electrode and performed XPS measurements. F.H., X.C., Y.L., and Y.Y. wrote the manuscript with the input of all authors.

DECLARATION OF INTERESTS

The authors declare no competing interests.

Received: December 13, 2018

Revised: February 19, 2019

Accepted: March 15, 2019

Published: April 19, 2019

REFERENCES

1. Zhao, C., Liu, L., Qi, X., Lu, Y., Wu, F., Zhao, J., Yu, Y., Hu, Y.S., and Chen, L. (2018). Solid-state sodium batteries. *Adv. Energy Mater.* **8**, 1703012.
2. Janek, J., and Zeier, W.G. (2016). A solid future for battery development. *Nat. Energy* **1**, 16141.
3. Lu, Y., Li, L., Zhang, Q., Niu, Z., and Chen, J. (2018). Electrolyte and interface engineering for solid-state sodium batteries. *Joule* **2**, 1747–1770.
4. Kim, J.-J., Yoon, K., Park, I., and Kang, K. (2017). Progress in the development of sodium-ion solid electrolytes. *Small Methods* **1**, 1700219.
5. Duchardt, M., Ruschewitz, U., Adams, S., Dehnen, S., and Roling, B. (2018). Vacancy-controlled Na⁺ superion conduction in Na₁₁Sn₂PS₁₂. *Angew. Chem. Int. Ed.* **57**, 1351–1355.
6. Hayashi, A., Noi, K., Sakuda, A., and Tatsumisago, M. (2012). Superionic glass-ceramic electrolytes for room-temperature rechargeable sodium batteries. *Nat. Commun.* **3**, 856.
7. Nose, M., Kato, A., Sakuda, A., Hayashi, A., and Tatsumisago, M. (2015). Evaluation of mechanical properties of Na₂S–P₂S₅ sulfide glass electrolytes. *J. Mater. Chem. A* **3**, 22061–22065.
8. Tian, Y., Shi, T., Richards, W.D., Li, J., Kim, J.C., Bo, S.-H., and Ceder, G. (2017). Compatibility issues between electrodes and electrolytes in solid-state batteries. *Energy Environ. Sci.* **10**, 1150–1166.
9. Kim, S.W., Seo, D.H., Ma, X., Ceder, G., and Kang, K. (2012). Electrode materials for rechargeable sodium-ion batteries: potential alternatives to current lithium-ion batteries. *Adv. Energy Mater.* **2**, 710–721.
10. Pan, H., Hu, Y.-S., and Chen, L. (2013). Room-temperature stationary sodium-ion batteries for large-scale electric energy storage. *Energy Environ. Sci.* **6**, 2338–2360.
11. Banerjee, A., Park, K.H., Heo, J.W., Nam, Y.J., Moon, C.K., Oh, S.M., Hong, S.-T., and Jung, Y.S. (2016). Na₃SbS₄: a solution processable sodium superionic conductor for all-solid-state sodium-ion batteries. *Angew. Chem.* **128**, 9786–9790.
12. Hayashi, A., Noi, K., Tanibata, N., Nagao, M., and Tatsumisago, M. (2014). High sodium ion conductivity of glass-ceramic electrolytes with cubic Na₃PS₄. *J. Power Sources* **258**, 420–423.
13. Han, F., Zhu, Y., He, X., Mo, Y., and Wang, C. (2016). Electrochemical stability of Li₁₀GeP₂S₁₂

- and $\text{Li}_7\text{La}_3\text{Zr}_2\text{O}_{12}$ solid electrolytes. *Adv. Energy Mater.* **6**, 1501590.
14. Zhang, W., Leichtweiß, T., Culver, S.P., Koerver, R., Das, D., Weber, D.A., Zeier, W.G., and Janek, J. (2017). The detrimental effects of carbon additives in $\text{Li}_{10}\text{GeP}_2\text{S}_{12}$ -based solid-state batteries. *ACS Appl. Mater. Interfaces* **9**, 35888–35896.
 15. Tang, H., Deng, Z., Lin, Z., Wang, Z., Chu, I.-H., Chen, C., Zhu, Z., Zheng, C., and Ong, S.P. (2018). Probing solid–solid interfacial reactions in all-solid-state sodium-ion batteries with first-principles calculations. *Chem. Mater.* **30**, 163–173.
 16. Ohta, N., Takada, K., Sakaguchi, I., Zhang, L., Ma, R., Fukuda, K., Osada, M., and Sasaki, T. (2007). LiNbO_3 -coated LiCoO_2 as cathode material for all solid-state lithium secondary batteries. *Electrochem. Commun.* **9**, 1486–1490.
 17. Li, X., Liu, J., Banis, M.N., Lushington, A., Li, R., Cai, M., and Sun, X. (2014). Atomic layer deposition of solid-state electrolyte coated cathode materials with superior high-voltage cycling behavior for lithium ion battery application. *Energy Environ. Sci.* **7**, 768–778.
 18. Xu, R., Sun, H., de Vasconcelos, L.S., and Zhao, K. (2017). Mechanical and structural degradation of $\text{LiNi}_x\text{Mn}_y\text{Co}_z\text{O}_2$ cathode in Li-ion batteries: an experimental study. *J. Electrochem. Soc.* **164**, A3333–A3341.
 19. Koerver, R., Ayyüñ, I., Leichtweiß, T., Dietrich, C., Zhang, W., Binder, J.O., Hartmann, P., Zeier, W.G., and Janek, J. (2017). Capacity fade in solid-state batteries: interphase formation and chemomechanical processes in nickel-rich layered oxide cathodes and lithium thiophosphate solid electrolytes. *Chem. Mater.* **29**, 5574–5582.
 20. Koerver, R., Zhang, W., de Biasi, L., Schweidler, S., Kondrakov, A.O., Kolling, S., Brezesinski, T., Hartmann, P., Zeier, W.G., and Janek, J. (2018). Chemo-mechanical expansion of lithium electrode materials – on the route to mechanically optimized all-solid-state batteries. *Energy Environ. Sci.* **11**, 2142–2158.
 21. Hao, F., Han, F., Liang, Y., Wang, C., and Yao, Y. (2018). Architectural design and fabrication approaches for solid-state batteries. *MRS Bull.* **43**, 775–781.
 22. Zhao, Q., Lu, Y., and Chen, J. (2017). Advanced organic electrode materials for rechargeable sodium-ion batteries. *Adv. Energy Mater.* **7**, 1601792.
 23. Jing, Y., Liang, Y., Gheyhani, S., and Yao, Y. (2017). Cross-conjugated oligomeric quinones for high performance organic batteries. *Nano Energy* **37**, 46–52.
 24. Liang, Y., Jing, Y., Gheyhani, S., Lee, K.Y., Liu, P., Facchetti, A., and Yao, Y. (2017). Universal quinone electrodes for long cycle life aqueous rechargeable batteries. *Nat. Mater.* **16**, 841–848.
 25. Liang, Y., and Yao, Y. (2018). Positioning organic electrode materials in the battery landscape. *Joule* **2**, 1690–1706.
 26. Chi, X., Liang, Y., Hao, F., Zhang, Y., Whiteley, J., Dong, H., Hu, P., Lee, S., and Yao, Y. (2018). Tailored organic electrode material compatible with sulfide electrolyte for stable all-solid-state sodium batteries. *Angew. Chem. Int. Ed.* **57**, 2630–2634.
 27. Nokami, T., Matsuo, T., Inatomi, Y., Hojo, N., Tsukagoshi, T., Yoshizawa, H., Shimizu, A., Kuramoto, H., Komae, K., Tsuyama, H., et al. (2012). Polymer-bound pyrene-4,5,9,10-tetraone for fast-charge and -discharge lithium-ion batteries with high capacity. *J. Am. Chem. Soc.* **134**, 19694–19700.
 28. Liang, Y., Zhang, P., and Chen, J. (2013). Function-oriented design of conjugated carbonyl compound electrodes for high energy lithium batteries. *Chem. Sci.* **4**, 1330–1337.
 29. McGrogan, F.P., Swamy, T., Bishop, S.R., Eggleton, E., Porz, L., Chen, X., Chiang, Y.-M., and Van Vliet, K.J. (2017). Compliant yet brittle mechanical behavior of $\text{Li}_2\text{S}-\text{P}_2\text{S}_5$ lithium-ion-conducting solid electrolyte. *Adv. Energy Mater.* **7**, 1602011.
 30. Ho, C., Raistrick, I.D., and Huggins, R.A. (1980). Application of A-C techniques to the study of lithium diffusion in tungsten trioxide thin films. *J. Electrochem. Soc.* **127**, 343–350.
 31. Tanibata, N., Deguchi, M., Hayashi, A., and Tatsumisago, M. (2017). All-solid-state Na/S batteries with a Na_3PS_4 electrolyte operating at room temperature. *Chem. Mater.* **29**, 5232–5238.
 32. Wenzel, S., Leichtweiss, T., Weber, D.A., Sann, J., Zeier, W.G., and Janek, J. (2016). Interfacial reactivity benchmarking of the sodium ion conductors Na_3PS_4 and sodium β -alumina for protected sodium metal anodes and sodium all-solid-state batteries. *ACS Appl. Mater. Interfaces* **8**, 28216–28224.
 33. Koerver, R., Walther, F., Ayyüñ, I., Sann, J., Dietrich, C., Zeier, W.G., and Janek, J. (2017). Redox-active cathode interphases in solid-state batteries. *J. Mater. Chem. A* **5**, 22750–22760.
 34. Duchêne, L., Kühnel, R.-S., Stilp, E., Cuervo Reyes, E., Remhof, A., Hagemann, H., and Battaglia, C. (2017). A stable 3 V all-solid-state sodium-ion battery based on a closo-borate electrolyte. *Energy Environ. Sci.* **10**, 2609–2615.
 35. Wang, Y., Ding, Y., Pan, L., Shi, Y., Yue, Z., Shi, Y., and Yu, G. (2016). Understanding the size-dependent sodium storage properties of $\text{Na}_2\text{C}_6\text{O}_6$ -based organic electrodes for sodium-ion batteries. *Nano Lett.* **16**, 3329–3334.
 36. Yue, J., Han, F., Fan, X., Zhu, X., Ma, Z., Yang, J., and Wang, C. (2017). High-performance all-inorganic solid-state sodium–sulfur battery. *ACS Nano* **11**, 4885–4891.
 37. Gao, Y., Wang, D., Li, Y.C., Yu, Z., Mallouk, T.E., and Wang, D. (2018). Salt-based organic–inorganic nanocomposites: towards a stable lithium metal/ $\text{Li}_{10}\text{GeP}_2\text{S}_{12}$ solid electrolyte interface. *Angew. Chem. Int. Ed.* **57**, 13608–13612.
 38. Chevrier, V.L., and Ceder, G. (2011). Challenges for Na-ion negative electrodes. *J. Electrochem. Soc.* **158**, A1011–A1014.
 39. Oliver, W.C., and Pharr, G.M. (1992). An improved technique for determining hardness and elastic modulus using load and displacement sensing indentation experiments. *J. Mater. Res.* **7**, 1564–1583.
 40. Chu, I.H., Kompella, C.S., Nguyen, H., Zhu, Z., Hy, S., Deng, Z., Meng, Y.S., and Ong, S.P. (2016). Room-temperature all-solid-state rechargeable sodium-ion batteries with a Cl-doped Na_3PS_4 superionic conductor. *Sci. Rep.* **6**, 33733.
 41. Yu, Z., Shang, S.-L., Seo, J.-H., Wang, D., Luo, X., Huang, Q., Chen, S., Lu, J., Li, X., Liu, Z.-K., et al. (2017). Exceptionally high ionic conductivity in $\text{Na}_3\text{P}_{0.62}\text{As}_{0.38}\text{S}_4$ with improved moisture stability for solid-state sodium-ion batteries. *Adv. Mater.* **29**, 1605561.
 42. Heo, J.W., Banerjee, A., Park, K.H., Jung, Y.S., and Hong, S.-T. (2018). New Na-ion solid electrolytes $\text{Na}_{4-x}\text{Sn}_{1-x}\text{Sb}_x\text{S}_4$ ($0.02 \leq x \leq 0.33$) for all-solid-state Na-ion batteries. *Adv. Energy Mater.* **8**, 1702716.
 43. Moon, C.K., Lee, H.-J., Park, K.H., Kwak, H., Heo, J.W., Choi, K., Yang, H., Kim, M.-S., Hong, S.-T., Lee, J.H., et al. (2018). Vacancy-driven Na^+ superionic conduction in new Ca-doped Na_3PS_4 for all-solid-state Na-ion batteries. *ACS Energy Lett.* **3**, 2504–2512.
 44. Li, Y., Deng, Z., Peng, J., Chen, E., Yu, Y., Li, X., Luo, J., Huang, Y., Zhu, J., Fang, C., et al. (2018). A P2-type layered superionic conductor Ga-doped $\text{Na}_2\text{Zn}_2\text{TeO}_6$ for all-solid-state sodium-ion batteries. *Chemistry* **24**, 1057–1061.
 45. Zhang, Z., Zhang, Q., Shi, J., Chu, Y.S., Yu, X., Xu, K., Ge, M., Yan, H., Li, W., Gu, L., et al. (2017). A self-forming composite electrolyte for solid-state sodium battery with ultralong cycle life. *Adv. Energy Mater.* **7**, 1601196.
 46. Kim, J.-K., Lim, Y.J., Kim, H., Cho, G.-B., and Kim, Y. (2015). A hybrid solid electrolyte for flexible solid-state sodium batteries. *Energy Environ. Sci.* **8**, 3589–3596.
 47. Rao, R.P., Chen, H., Wong, L.L., and Adams, S. (2017). $\text{Na}_{3+x}\text{M}_x\text{P}_{1-x}\text{S}_4$ ($\text{M} = \text{Ge}^{4+}, \text{Ti}^{4+}, \text{Sn}^{4+}$) enables high rate all-solid-state Na-ion batteries $\text{Na}_{2+2\delta}\text{Fe}_{2-2\delta}(\text{SO}_4)_3[\text{Na}_{3+x}\text{M}_x\text{P}_{1-x}\text{S}_4][\text{Na}_2\text{Ti}_3\text{O}_7]$. *J. Mater. Chem. A* **5**, 3377–3388.